Journal of Alloys and Compounds 861 (2021) 158630

Contents lists available at ScienceDirect

Journal of Alloys and Compounds

journal homepage: www.elsevier.com/locate/jalcom

Phase field model for multiphase alloys under arbitrary thermal history: An application to IN718 super-alloy

Robert Laskowski*, Kun Wang, Rajeev Ahluwalia, Kewu Bai, Guglielmo Vastola, Yong-Wei Zhang

*Institute of High Performance Computing, A*STAR, Singapore 138632, Singapore*

ARTICLE INFO

Article history:
Received 14 October 2020
Received in revised form 1 January 2021
Accepted 4 January 2021
Available online 6 January 2021

ABSTRACT

Currently, it is still a significant challenge to predict the microstructural evolution of multiphase alloys in complex manufacturing processes such as joining, welding and additive manufacturing due to their complex thermodynamics and thermal history. In this work, we present a phase-field framework, aiming to predict the evolution of precipitate microstructure under arbitrary thermal history. Our model incorporates nucleation, growth and transformation by taking into account interfacial, chemical and elastic energies. In order to quantitatively describe the nucleation of phases, we leverage on experimental time-temperature-transformation data to parameterize the classical nucleation model. For demonstration, we employ super-alloy IN718, where thermodynamic and kinetic data is obtained using CALPHAD method and major precipitate phases, i.e. γ', γ'' and δ and their variants are considered. The predicted continuous-cooling-transformation diagram is consistent with data existing in literature, thus validating the approach. We further predict the precipitate evolution under rapid thermal cycling to mimic a typical additive manufacturing process.

1. Introduction

Manufacturing processes, such as joining, welding and particularly additive manufacturing (AM), due to their unique processing/scanning strategies, experience complex thermal histories. From the point of view of the mechanical properties, it is important to understand precipitation in alloys under such conditions. For instance, in multi-phase alloys (MPA) it may be useful to determine which phase will be dominant at the end of the process. Fast thermal cycling during mentioned processes makes it difficult to experimentally monitor the precipitate evolution. In such cases, simulation models can provide useful insight.

Mean-field-based empirical methods, such as Johnson-Mehl-Avarami-Kolmogorov (JMAK) [1–3] or CALPHAD-based [4] are routinely used to simulate kinetics of precipitate formation in MPA. For instance, the commercial code JMATPRO is used to compute the time-temperature-transformation (TTT) and continuous-cooling-transformation (CCT) diagrams for a large number of systems [5]. For a case with arbitrary thermal history, one usually refers to additivity principle dividing a process into small isothermal steps [3]. It should be noted that the mean-field-based methods, although attractive due to their computational simplicity, do not resolve the precipitate morphology. Furthermore, assumed local equilibrium conditions during precipitate evolution may be valid only for isothermal transformations or for continuous cooling with slow cooling rates.

Phase field method (PFM), on the other hand, offers a general simulation framework that is capable of predicting the transformation diagrams, precipitate morphologies [6–11], and takes into account local non-equilibrium conditions that arise due to fast heating/cooling. A key issue of microstructure models is to account for nucleation phenomena in quantitative manner. Although, the classical nucleation model (CNM) has been incorporated in the PFM [12,13], it is not clear how to parameterize it to achieve a reliable description of precipitate nucleation for a wide range of temperatures. Therefore we propose here, based on the assumption that reliable TTT diagrams is available, to parameterize the CNM such that these TTT diagrams can be properly reproduced. The derived model is then used to predict the precipitate nucleation in MPAs under an arbitrary thermal history.

In principle, PFM framework presented here can be applied to any MPA, but for demonstration, we choose a well-known nickel-based super-alloy IN718. This alloy has been widely used in

* Correspondence to: Institute of High Performance Computing, A*STAR, 1 Fusionopolis Way, #16-16, Connexis, Singapore 138632, Singapore.
E-mail address: rolask@ihpc-astar.edu.sg (R. Laskowski).

https://doi.org/10.1016/j.jallcom.2021.158630
0925-8388/

aerospace industry as well as nuclear power plants [14]. There are extensive experimental data available considering the type, composition and transformation of various phases [15–19], including TTT diagrams [20–22]. In IN718, nickel is primarily alloyed with elements such as Nb, Al, Fe, Cr and Mo. Face centered cubic, γ is the high temperature phase, the dominant precipitates are $\gamma''(D0_{22}$ tetragonal), γ' (Ll_2 cubic) and δ ($D0_a$ orthorhombic). During isothermal annealing, the stable δ precipitates first start to form at the grain boundaries [18], in the appropriate temperature range, the nucleation of γ'' and γ' precipitates occurs intragranularly [15,16]. The δ precipitates can be large plate shape, γ'' and γ'precipitates are smaller (~10–50 nm). The γ'' precipitates are disk-shaped while γ' precipitates are equiaxed or cuboidal. From a modeling point of view, mean-field-based approach [23,24] has been applied to predict precipitate evolution during selective laser melting, and PFM has been used to investigate the precipitate morphologies [8–10,25]. However the evolution of precipitate morphologies in IN718 during complex non-isothermal processes has not been addressed.

The present paper is organized as follows: The next section outlines the details of our PFM model. Thereafter, application to IN718 is discussed, the classical nucleation model and its parametrization using experimental TTT diagrams, the material properties, and the simulation model setup. After that, the PFM framework is employed to calculate CCT diagrams, and the predictions are compared with existing experimental results. Next, we discuss an example of its application to an arbitrary thermal cycling, that could be found in a typical AM process, and compare with existing experimental results and implications. The last section summarizes and concludes our work.

2. Phase field framework

Phase transformations in an alloy with an arbitrary number of product phases and their variants, as well arbitrary number of chemical components can be described by the multi-phase field model [8,11]. The order parameter is an N-component vector $\vec{n}$ (N is the total number of product phases/variants) such that product phase/variant m is represented by $n_{v=m} = 1$ and $n_{v\neq m} = 0$. The parent (matrix) phase is described by the case when all components of the order parameter vanish, i.e. $\vec{n} = 0$. Following the standard formulation, interfacial energy f_{int}, chemical free energy f_{chem} and the elastic energy associated with the phase transformations f_{el} constitute the free energy of the system:

$$F = \int dV\,(f_{int} + f_{chem} + f_{el}) \tag{1}$$

The interfacial contribution is expressed in terms of the order parameter using following expression:

$$f_{int} = \sum_v \left(W_v n_v^2 (1 - n_v)^2 + \frac{K_v}{2} (\nabla n_v)^2 \right) + \xi \sum_{v \neq v'} n_v^2 n_{v'}^2 \tag{2}$$

The summation runs over all product phases and their variants. The barrier height W_v and the gradient coefficients K_v are related to the interfacial energies and interfacial widths between v phase precipitates and γ phase [8] (note that the variants of the same phase will have the same values of the constants W_v and K_v). The last term in Eq. (2) ensures that for a large enough value of ξ, only one of the N components of order parameter vector $\vec{n}$ is non-zero.

The chemical portion of the free energy is written as:

$$f_{chem} = \frac{1}{V_m} \left(1 - \sum_v h(n_v) \right) G_0(\vec{X_0}) + \frac{1}{V_m} \sum_v h(n_v) G_v(\vec{X_v}) \tag{3}$$

Here $h(n_v) = n_v^3(6n_v^2 - 15n_v + 10)$ is an interpolating function, V_m is the molar volume, and G_v is the Gibbs free energy of phase v. Variants of a particular phase share the same functional form of G_v (for simplicity, the notation in Eq. (3) does not indicate this). Following the method introduced by Kim et al. [26], $\vec{X_v}$ represents the vector of auxiliary composition variables. The auxiliary composition vectors for all phases are obtained from the actual composition field by solving the following set of equations:

$$\frac{\partial G_0}{\partial X_{c,0}} = \frac{\partial G_v}{\partial X_{c,v}} = \bar{\mu}_c \tag{4}$$

$$x_c = \left(1 - \sum_v h(n_v) \right) X_{c,0} + \left(\sum_v h(n_v) X_{c,v} \right) \tag{5}$$

In both equations, index c covers independent composition variables, and x_c is the actual composition field, index *0* corresponds to the matrix phase. Eq. (4) assumes equality of the diffusion potentials $\bar{\mu}_c$ among all phases for independent components variables in the matrix of the dependent component variable. Eq. (5) normalizes the composition field across different phases to the actual value.

The structural transformation during precipitation generates strains that may substantially change the free energy. The elastic energy in a general case is expressed as

$$f_{el} = \frac{1}{2} \sum_{ijkl} C_{ijkl} e_{ij} e_{kl}. \tag{6}$$

Elastic tensor C_{ijkl} and strain tensor e_{ij} fields are interpolated between known values for each phase:

$$C_{ijkl} = \left(1 - \sum_v h(n_v) \right) C^{\gamma}_{ijkl} + \left(\sum_v h(n_v) C^{v}_{ijkl} \right) \tag{7}$$

$$e_{ij} = \varepsilon_{ij} - \left(\sum_v h(n_v) \varepsilon^{v}_{ijkl} \right) - \delta_{ij} \varepsilon_{th} \tag{8}$$

Here ε^v_{ij} are the components of transformation strain tensor for the v phase/variant, ε_{th} represents thermal strain. The strain tensor is calculated by using the displacement fields u_i as $\varepsilon_{ij} = 1/2(\partial u_i/\partial x_j + \partial u_j/\partial x_i) + \bar{\varepsilon}_{ij}$ and the stress tensor is calculated as $\sigma_{ij} = \partial f_{el}/\partial \varepsilon_{ij}$. For a macroscopically stress-free system, $\bar{\varepsilon}_{ij}$ is chosen such that all stress components average to zero.

The kinetics of the transformation is described by the usual set of equations:

$$\frac{1}{\Gamma_v} \frac{\partial n_v}{\partial t} = -\frac{\delta (f_{int} + f_{chem} + f_{el})}{\delta n_v} \tag{9}$$

$$\frac{\partial x_c}{\partial t} = -\vec{\nabla} \cdot \left(\sum_{c'} L_{cc'} \vec{\nabla} \bar{\mu}_c \right), \quad L_{cc'} = \sum_{c''} (\delta_{cc''} - x_c)(\delta_{c'c''} - x_{c'}) x_{c''} M_{c''} \tag{10}$$

$$\frac{\partial \sigma_{ij}}{\partial x_i} = 0, \quad \sigma_{ij} = \frac{\partial f_{el}}{\partial \varepsilon_{ij}} \tag{11}$$

Eq. (9) describes the evolution of the order parameter and Γ_v is the interfacial mobility. Eq. (10) is the standard multi-component diffusion equations that describe the evolution of compositions [27]. Here M_c is the atomic mobility that can be obtained from kinetic databases. Eq. (11) represents the mechanical equilibrium condition that is used to calculate the elastic strains.

3. Parameters for IN718

Incorporating all the chemical components and phases present in IN718 in our PFM framework is a numerically challenging task. However, it can be simplified by focusing on selected phases and applying surrogate composition approximation [28], in which the composition variables are grouped according to phases they

stabilize. Considering IN718, we take into account only major phases known to affect its mechanical properties namelyγ'', γ' and δ. Following this, we adopt a surrogate ternary approximation (Ni-{Al}-{Nb}), where {Al} represents γ' stabilizers, {Nb} represents γ'' and δ stabilizers, and Ni is considered as itself. The reader is referred to Supplementary Materials for more details.

Eqs. (11) are solved using finite difference methods for a macroscopically stress free system with periodic boundary conditions. The mechanical equilibrium condition is solved in real space in terms of the displacement fields, using the iterative method. All simulations reported in this work are carried out on $128 \times 128 \times 128$ grid with a grid spacing of 5 nm. Representative volume element (RVE) of size $0.64\,\mu m \times 0.64\,\mu m \times 0.64\,\mu m$ allows to describe small γ'precipitates (size close to 50 nm) and larger γ''plates (size from 100 nm to 600 nm). Time step is dynamically adjusted by monitoring change of the order parameters and composition variables. The initial condition corresponds to the nominal composition of IN718, i.e. $X_{\gamma,Al} = x_{Al} = 0.024$ and $X_{\gamma,Nb} = x_{Nb} = 0.038$. Our surrogate ternary approximation is parameterized using CALPHAD approach (see Supplementary Materials for more details). It should be noted that equilibrium phase relations given by surrogate ternary Gibbs free energies among all considered phases are consistent with the IN718 phase diagram. Additional parameters are obtained from existing literature. Table 1 summarizes the thermodynamic, interfacial, kinetic properties. Transformation strains are given in Table 2. The elastic tensors used in the simulations are shown in Table 3.

Although our model is partially derived from the work of Zhou et al. [8], there are some significant differences. In terms of the phase field model, the present work takes into account all important phases and their variants. In comparison, Refs. [9,10] only described the γ- γ'- γ'' system. Although Ref. [8] took into account the formation of, only one variant was considered. The most important new feature of the present model is the capability to describe complex non-isothermal processes. Unlike earlier works [8–10] that were focused primarily on isothermal transformations and precipitate morphologies, the aim of the present work is to develop an approach that can be applied to arbitrary complex thermal histories. To describe such processes, we have generalized the models so that non-isothermal processes can be described. In addition to the temperature-dependent thermodynamic and kinetic models, the most important new feature is the incorporation of a nucleation model that is consistent with its experimental TTT curve. This has not been accounted for in any of the earlier phase field studies. Incorporation of this quantitative nucleation model allows us to apply our model to complex thermal processes. The nucleation model and its parameterization using TTT curves are described in Sections 4 and 5.

4. The classical nucleation model

The classical nucleation theory [30] estimates the nucleation rates (number of nuclei per unit volume per unit time) from parent to each product phase v with the following expression:

Table 2
Transformation strains in basis $[100]_\gamma$, $[010]_\gamma$ and $[001]_\gamma$ Ref. [8].

$$\begin{bmatrix} -0.003 & 0 & 0 \\ 0 & -0.003 & 0 \\ 0 & 0 & -0.003 \end{bmatrix}_{\gamma'}$$

$$\begin{bmatrix} 0.0286 & 0 & 0 \\ 0 & 0.0067 & 0 \\ 0 & 0 & 0.0067 \end{bmatrix}_{\gamma_1'} \quad \begin{bmatrix} 0.0110 & 0.0057 & -0.0035 \\ 0.0057 & 0.0110 & -0.0035 \\ -0.0035 & -0.0035 & 0.0202 \end{bmatrix}_{\delta_1}$$

+ 2 symmetry eqivalents + 11 symmetry eqivalents

Table 3
Elastic constants in basis $[100]_\gamma$, $[010]_\gamma$ and $[001]_\gamma$ (MPa) Ref. [29].

$$\begin{bmatrix} 276 & 159 & 159 & 0 & 0 & 0 \\ 159 & 276 & 159 & 0 & 0 & 0 \\ 159 & 159 & 276 & 0 & 0 & 0 \\ 0 & 0 & 0 & 132 & 0 & 0 \\ 0 & 0 & 0 & 0 & 132 & 0 \\ 0 & 0 & 0 & 0 & 0 & 132 \end{bmatrix}_{\gamma} \quad \begin{bmatrix} 238 & 147 & 147 & 0 & 0 & 0 \\ 159 & 238 & 147 & 0 & 0 & 0 \\ 147 & 147 & 238 & 0 & 0 & 0 \\ 0 & 0 & 0 & 129 & 0 & 0 \\ 0 & 0 & 0 & 0 & 129 & 0 \\ 0 & 0 & 0 & 0 & 0 & 129 \end{bmatrix}_{\gamma'}$$

$$\begin{bmatrix} 286 & 181 & 160 & 0 & 0 & 0 \\ 181 & 286 & 160 & 0 & 0 & 0 \\ 160 & 181 & 308 & 0 & 0 & 0 \\ 0 & 0 & 0 & 112 & 0 & 0 \\ 0 & 0 & 0 & 0 & 112 & 0 \\ 0 & 0 & 0 & 0 & 0 & 116 \end{bmatrix}_{\gamma_1'}$$

+ 2 symmetry equivalents

$$\begin{bmatrix} 308.06 & 166.22 & 159.39 & 2.72 & -5.11 & 16.06 \\ 166.22 & 298.22 & 166.22 & -9.11 & 16.89 & -9.11 \\ 159.39 & 166.22 & 308.06 & 16.06 & -5.11 & 2.72 \\ 2.72 & -9.11 & 16.06 & 87.89 & 9.06 & 84.06 \\ -5.11 & 16.89 & -5.11 & 9.06 & 84.06 & 9.06 \\ 16.06 & -9.11 & 2.72 & 20.22 & 9.06 & 87.89 \end{bmatrix}_{\delta_1}$$

+ 11 symmetry equivalents

$$J_v = N_v \frac{2V_m}{N_A\sqrt{k_bT}} \frac{\sqrt{\gamma_v} D_v^{eff}}{a^4} exp\left(-f_v \frac{16\pi {\gamma_v}^3}{3(\Delta G_{nuc}^v)^2 k_b T}\right) \tag{12}$$

where N_A, V_m, k_bT, a are the Avogadro's number, molar volume, Boltzmann temperature factor and the matrix crystal lattice spacing, γ_v is the interfacial energy between parent and product v phase. The effective diffusivity D_v^{eff} is calculated using the formula [31]:

$$D_v^{eff} = \left(\sum_c \frac{(X_{c,v}^{eq} - X_{c,0})^2}{X_{c,0} R T M_{c,0}}\right)^{-1} \tag{13}$$

$M_{c,0}$ is the atomic mobility in the parent phase, and ΔG_{nuc}^v is the driving force for nucleation of v phase approximated by:

$$\Delta G_{nuc}^v = \frac{1}{V_m} \sum_c X_{c,v}^{eq} (\mu_c^0(\vec{X}_0) - \mu_c^v(\vec{X}_v^{eq})) \tag{14}$$

Here $\mu_c^0(\vec{X}_0)$ is the chemical potential of component c in the parent phase at the actual composition and $\mu_c^v(\vec{X}_v^{eq})$ is the chemical potential of component c in the product phase v at its equilibrium composition. The chemical potentials are evaluated using:

Table 1
Thermodynamic, interfacial and kinetic material properties used in the simulations.

Gibbs energies, G_v	G_γ, $G_{\gamma'}$, $G_{\gamma''}$, G_δ obtained from our surrogate ternary database seeSupplementary Materials
Gradient coefficient, K_v	$K_{\gamma'} = 6.2 \times 10^{-10}\frac{J}{m}$, $K_{\gamma''} = 1.24 \times 10^{-9}\frac{J}{m}$, $K_\delta = 1.24 \times 10^{-9}\frac{J}{m}$, Ref. [8]
Interfacial energies, γ_v	$\gamma_{\gamma'} = 0.0505$, $\gamma_{\gamma''} = 0.105$, $\gamma_\delta = 1.0$, Ref. [8]
Barriers, W_v	$W_{\gamma'} = 7.45 \times 10^7\frac{J}{m^3}$, $W_{\gamma''} = 1.49 \times 10^8\frac{J}{m^3}$, $W_\delta = 1.49 \times 10^9\frac{J}{m^3}$, Ref. [8]
Coupling coefficient ξ	$\xi = 1.07 \times 10^{11}$ Ref. [8]
Atomic mobility M_c	Redlich-Kister form (the reader is referred to the Supplementary Materials)
Interfacial mobility Γ_v	$\Gamma_{\gamma'} = \Gamma_{\gamma'} = \Gamma_{\gamma''} = \Gamma_\delta = 2.904 \times 10^{-11}\frac{m^2}{Ns}$ [8]

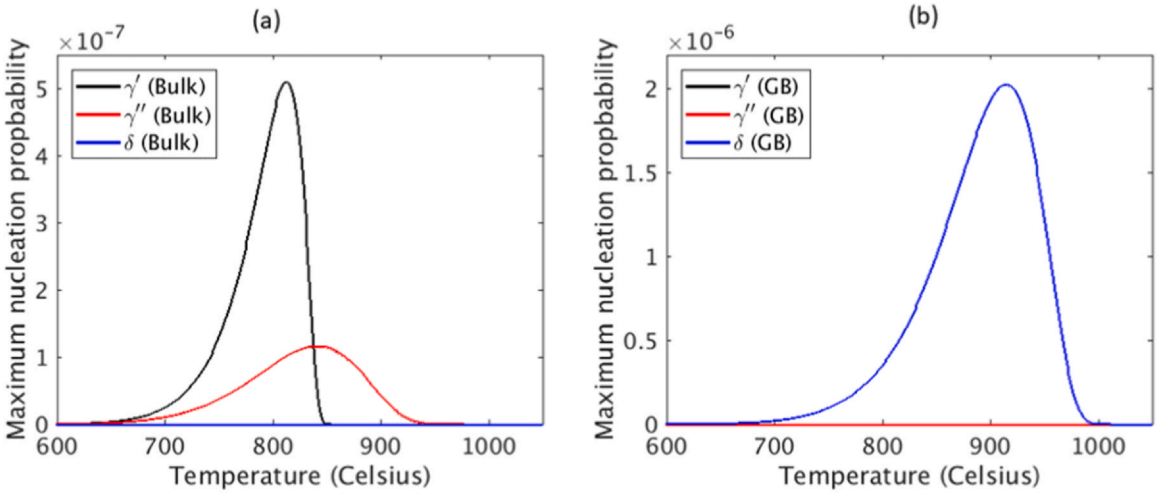

Fig. 1. Nucleation probabilities as a function of temperature obtained using values of N_v and f_v parameters listed Table 2. (a) shows the bulk case and (b) corresponds to the grain boundary nucleation.

$$\mu_c^v = G_v + (1 - X_{c,v})\frac{\partial G_v}{\partial X_{c,v}} - \sum_{c' \neq c}\left(X_{c',v}\frac{\partial G_v}{\partial X_{c',v}}\right) \tag{15}$$

In our approach, the parameters f_v and N_v are considered adjustable and are used to match our calculated TTT diagrams to the measured diagrams known from literature. The probability of seeding a nuclei of phase v at a grid point in a RVE is related to nucleation rates:

$$P_v = 1 - exp(-J_v \Delta t \Delta V) \tag{16}$$

where Δt and ΔV are the time step of the phase evolution solver and the volume of a single grid point, respectively.

The temperature dependence of J_v and P_v resembles a "bell shaped" curve (see Fig. 1). The position of the peak can be controlled by the value of f_v, N_v affects its height while the spread is determined by the driving force. In a recent work in the context of titanium alloys, a similar approach was adopted, where the nucleation parameters were tuned such that the experimental critical cooling rate above which no precipitation occurs can be reproduced in continuous cooling simulations [11]. A more systematic approach is adopted in the present work, where temperature dependence of P_v is adjusted to the proper temperature ranges in the experimental TTT diagrams. The time at which a given phase appears in those diagrams can be controlled by the value of P_v at its peak.

5. Parametrization of CNM in grain and at grain boundary by TTT diagrams

Nucleation of δ precipitates in IN718 initially occurs only at grain boundaries, whereas γ' and γ'' nucleate in the bulk. Typical grain sizes are of the order of several microns while the precipitate sizes are in the nanometer range. Therefore, it is not feasible to describe grain boundary phenomena and bulk precipitation processes in a single simulation domain. In order to consider polycrystalline nature of IN718, we introduce two different representative volume elements (RVEs): one represents a region deep inside a grain (bulk RVE), while the other is in the vicinity of a grain boundary (grain boundary RVE). The grain boundary is incorporated by introducing a special plane where the nucleation rate (i.e. values of N_v and f_v) is different from that in the bulk.

The phase field equations described in Section 2 are solved for isothermal conditions at selected temperatures in the range from 500 °C to 1000 °C, starting with pure γ phase. At each temperature, phase fractions (a phase is defined as the local value of the order parameter n_i is greater than 0.5) are monitored as a function of time, from which the TTT diagrams can be composed. The parameters f_v and N_v are chosen such that simulated TTT diagrams match the experimental TTT curves. There are, however, noticeable discrepancies among available experimental data. For instance, the diagrams from Refs. [20–22] do not separate γ' and γ'', indicating that those phases form simultaneously, while Ref. [22] suggests that γ' forms at much later times compared to γ''. It is likely that these differences may arise due to the variations in processing conditions as well the methodology used to determine the presence of precipitates. For the purpose of presentation, we intended to match our calculated diagrams with the curves from Ref. [20] (solid lines in TTT curves of Figs. 2 and 3).

The optimal values of N_v and f_v for bulk and grain boundary regions are shown in Table 4. Fig. 1 shows the corresponding nucleation probabilities as function of temperature, calculated at nominal composition. Note that the bulk nucleation rate for δ phase is very small due to high interfacial energy (around 10 times higher than that for γ''). The resulting TTT diagrams and experimental curves are shown in Fig. 2 for the bulk RVE and Fig. 3 for the grain boundary RVE. The TTT diagrams calculated in the present work are presented as maps of the phase fractions in temperature-time coordinates. Experimental TTT curves indicate "emergence" of a particular phase at a given time and temperature. Non monotonic behavior in the time evolution of the γ' phase fraction in the low temperature range T = 550–600 °C can be attributed to the effects associated with a transient decrease in the order parameter value due to the elastic misfit strains. The precipitate morphologies for bulk RVE after 10 h of isothermal hold are shown in Fig. 2(c-e). Only γ'' is observed at T = 850 °C, while a co-precipitation of $\gamma'$and γ'' is observed at T = 750 °C and T = 700 °C, which is consistent with the thermodynamic phase diagram of γ- $\gamma' - \gamma''$ system. Note that γ'' precipitates in Fig. 2(c-e) adopt the plate morphology with habit along $\{100\}_\gamma$ and the γ' precipitates have developed the usual cuboidal morphologies.

In order to compare the predictions of the model with experimental precipitate microstructures of IN718, we conducted a long time simulation for 100 h and also analyzed the evolution of precipitate sizes. Assuming an ellipsoidal geometry, the mean sizes of the precipitates are calculated using principal component analysis. Fig. 3(a) shows the time evolution of mean length and thickness of γ'' as well as the size of γ' at T = 750 °C. After a transient period where precipitates undergo shape relaxation, the precipitate sizes start growing steadily. After 10 h ageing, γ'' precipitate mean length

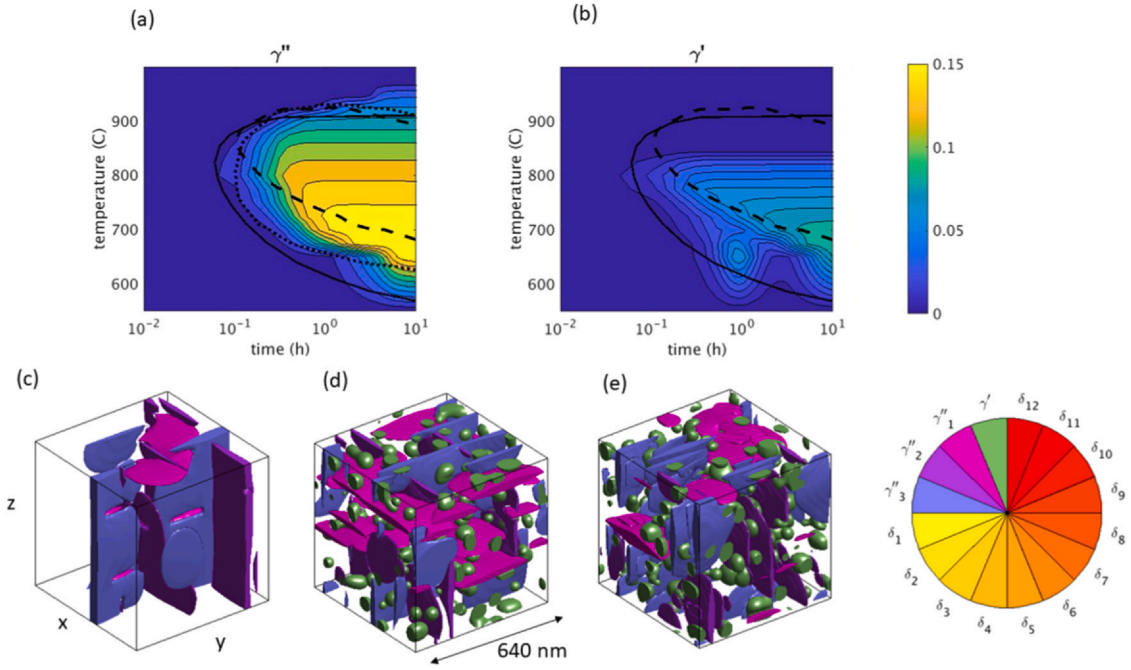

Fig. 2. Calculated TTT diagrams for γ'' (a) and γ' (b) for the bulk RVE. The shades in (a) and (b) represent phase fractions. Experimental TTT curves are displayed for comparison. The solid line in (a)-(b) corresponds to the combined $\gamma' + \gamma''$ curve from [20]. The dashed line in (a)-(b) corresponds to the combined $\gamma' + \gamma''$ curve from [21]. The dotted line in (a) corresponds to the γ'' curve from [22]. The precipitate microstructures after 10 h of isothermal annealing are shown for T = 850 °C (c), T = 750 °C (d) and T = 700 °C (e). The microstructures are shown in the basis X || $[100]_\gamma$, Y || $[010]_\gamma$ and Z || $[001]_\gamma$.

at T = 750 °C appears to saturate to range between ~260 and 290 nm (the small fluctuations are due to variant coalescence and shrinkage). The γ'' thickness saturates to ~25 nm. The mean γ' size grows to ~100 nm after 100 h ageing. The corresponding precipitate microstructure after 100 h of ageing is shown in Fig. 3(b). These results might be compared with corresponding experimental results from Ref. [32,33] where after ageing for 100 h at T = 750 °C, the γ'' precipitate length is ~120 nm according to [32] and ~190 nm according to [33], γ'' thickness is ~22 nm and γ' size is ~33 nm according to [32]. Clearly, our simulations predict a larger precipitate length of γ'', although the thicknesses are close to the experimental results. Similarly, size of simulated γ' precipitates is also larger compared to the experiments. These discrepancies could be due to the neglect of anti-phase domains for each variant/phase, which could restrict domain coalescence during coarsening and lead to smaller precipitate sizes. In principle, this can be included in the model, however at the cost of increasing computational complexity and time. Finally, uncertainty in kinetic parameters, such as interfacial mobility, can also contribute to the observed discrepancies.

Table 4
Nucleation model parameters for RVE for bulk and grain boundary.

	$f_{\gamma'}$	$f_{\gamma''}$	f_δ	$N_{\gamma'}[m^{-3}]$	$N_{\gamma''}[m^{-3}]$	$N_\delta[m^{-3}]$
bulk	0.08	0.2	1	3.9×10^{16}	1.17×10^{16}	3.9×10^{19}
grain boundary	1	1	0.00005	3.9×10^{9}	3.9×10^{9}	3.9×10^{15}

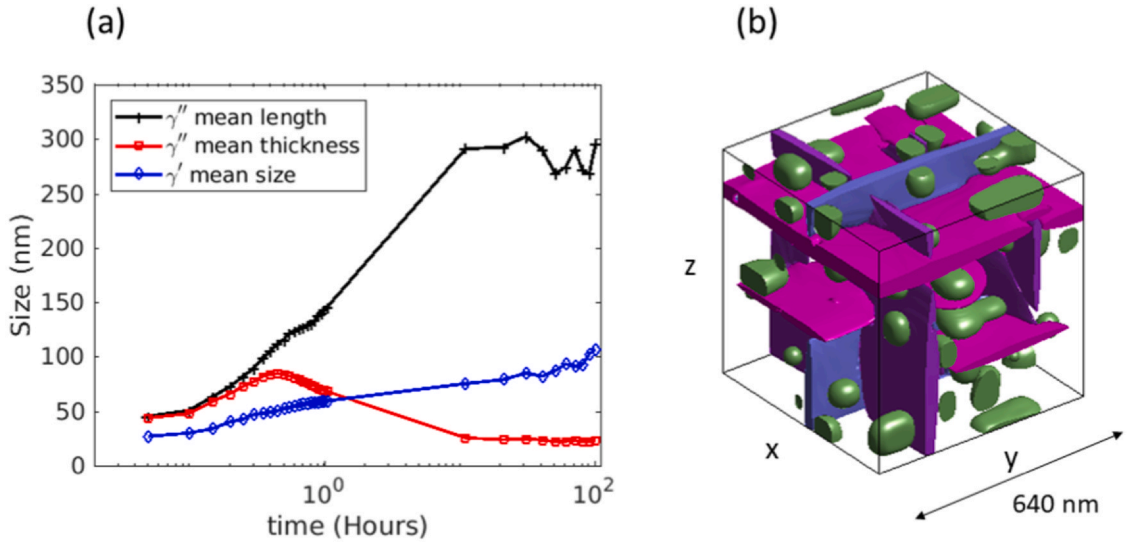

Fig. 3. (a) The time evolution precipitate sizes during isothermal hold at T = 750 °C and (b) the corresponding precipitate microstructure after 100 h. The microstructure is shown in the basis X || $[100]_\gamma$, Y || $[010]_\gamma$ and Z || $[001]_\gamma$.

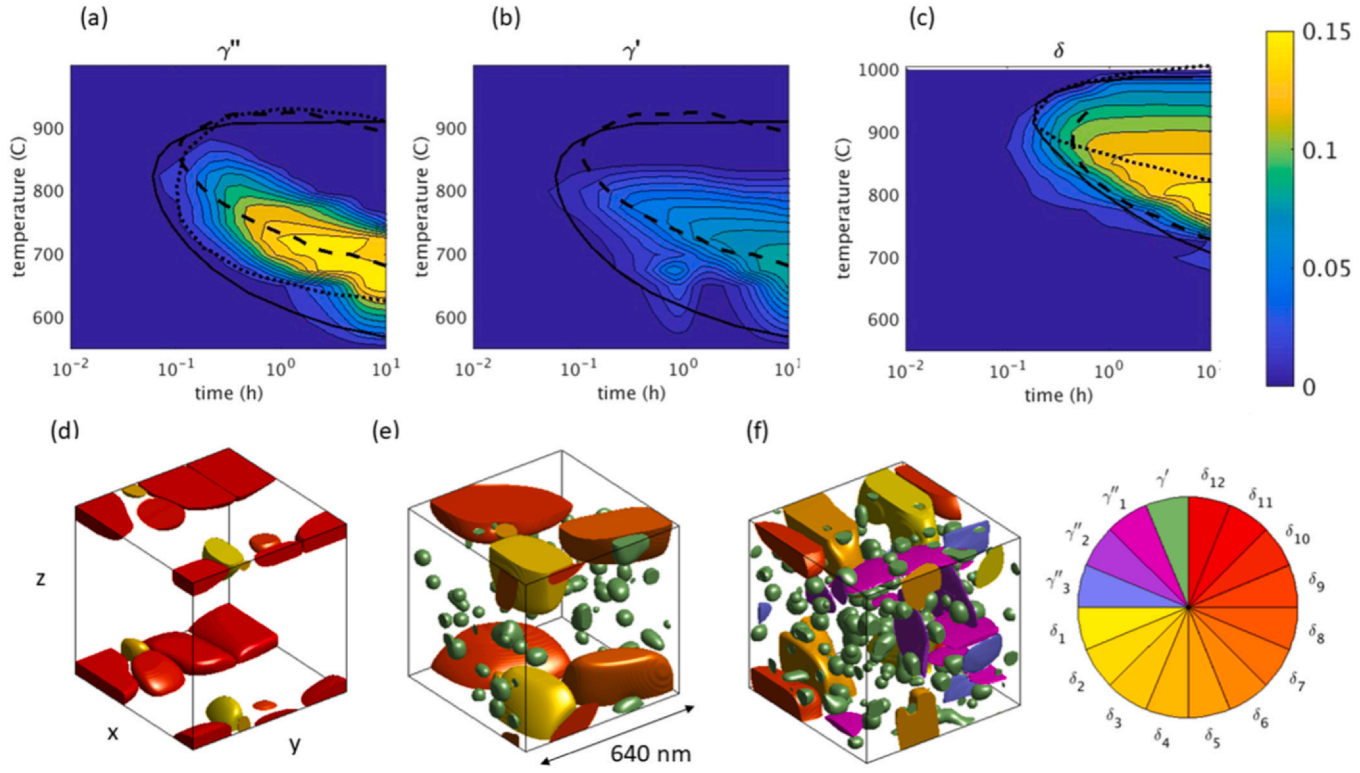

Fig. 4. Computed TTT diagrams for γ'' (a), γ' (b) and δ (c) for the RVE with grain boundary. The shades in (a), (b) and (c) represent phase fractions. Experimental TTT curves are displayed for comparison. The solid line in (a)-(b) corresponds to the combined $\gamma'+\gamma''$ curve from [20] while the solid line in (c) corresponds to the δ curve from the same reference. The dashed line in (a)-(b) corresponds to the combined $\gamma'+\gamma''$ curve from [21] while the dashed line in (c) corresponds to the δ curve from the same reference. The dotted line in (a) corresponds to the γ'' curve from [22] while the dotted line in (c) corresponds to the δ curve from the same reference. The precipitate microstructures after 10 h of isothermal annealing are shown for T = 950 °C (d), T = 800 °C (e) and T = 750 °C (f). The microstructures are shown in the basis X || $[100]_\gamma$, Y || $[010]_\gamma$ and Z || $[001]_\gamma$.

While the present work has been mostly concerned with benchmarking of nucleation model with TTT diagrams, future work should focus on benchmarking with TTT diagrams as well as precipitate sizes to develop a more predictive model.

In the case of RVE representing grain boundary region (Fig. 4), the transformation starting time is comparable with the experimental curves. The diagram for γ'' shows a clear negative slope at high temperatures. Since δ is the stable phase, its growth leads to the annihilation of initially-precipitated γ''. This effect is present in all experimental TTT curves [20–22], but in a less pronounced way. The decay of γ'' fraction in our simulations occurs at an earlier time and faster rate, compared to the experiments. This is due to the relatively small RVE volume, leading to an extremely high density of grain boundary. In principle, it should be possible to devise a procedure that would lead to a better fit in this case knowing the real value of grain boundary density. For instance, by interpolation between the results at grain boundary and in the interior of grains, or by simple extrapolation based on calculations with different RVE sizes. However, this exercise is beyond scope of this work. Fig. 4(d)-(f) show the precipitate morphologies after 10 h of annealing. At T = 950 °C, γ-δ coexistence is observed with the δ being localized at the grain boundary planes (d). A three-phase co-precipitation (γ- γ'- δ) is observed at T = 800 °C (e). Examining the simulated TTT curves, it is clear that this state is formed after an intermediate formation of γ'' that dissolves as the more stable δ domains grow at the grain boundary plane. At T = 750 °C, some γ'' precipitates still survive. Of course, after longer ageing than 10 h, the metastable γ'' precipitates disappear even at this temperature. δ precipitates do not exhibit the experimentally observed plate type morphology with habit along $\{111\}_\gamma$. This is likely due to the small size of the precipitates and the limited RVE size. In experiments, δ precipitates that emerge from grain boundaries are of lengths 2–5 μm, which is much bigger than the size of our RVE. Note that due to the small size of the RVE, we have not attempted to compare our results for this case with corresponding experimental results.

6. Prediction of CCT diagrams of IN718 and comparison with experiments

To compute CCT diagrams temperature is decreased from 1180 °C to 500 °C at different cooling rates, starting from γ phase. Time evolution of the phase fractions is monitored and a map of phase fractions in the time-temperature space is generated constituting our simulated CCT diagrams presented in Fig. 5 for bulk RVE and Fig. 6 for grain boundary RVE. It is seen that for a fast cooling rate, the γ' precipitates dominate, while a slower rate leads to the co-precipitation of γ- γ'- γ'' in bulk. These conclusions are qualitatively consistent with the published CCT curves for IN718 by Garcia et al. [34]. For both RVE cases, no phases reach 1% fraction for cooling rates faster then 4 °C/s. However, this does not mean that there are no precipitates, as seen in Fig. 5(c), even for cooling rate as high as 34 °C/s, traces of γ' can be found. A microstructure for the bulk case with a γ'-dominated microstructure corresponding to a cooling rate of 2.96 °C/s is shown in Fig. 5(d). γ- γ'- γ'' microstructure observed after cooling at rate of 0.03 °C/s is presented in Fig. 5(e). Note that γ'' precipitates are coarser and have adopted plate shape with habit on $\{100\}_\gamma$ planes. At the slowest cooling rate of 0.0041 °C/s, a large plate shaped γ'' is observed with cuboidal γ' as shown in Fig. 5(f).

For the grain boundary RVE (Fig. 6), in contrast to the bulk case, a co-precipitation of γ- γ'- δ is observed for slower cooling (Fig. 6c). Significant γ'' formation occurs only for a small range of intermediate cooling rates (Fig. 6b). A γ'dominated microstructure with a small number of δ precipitates is observed for 4.25 °C/s (d). For

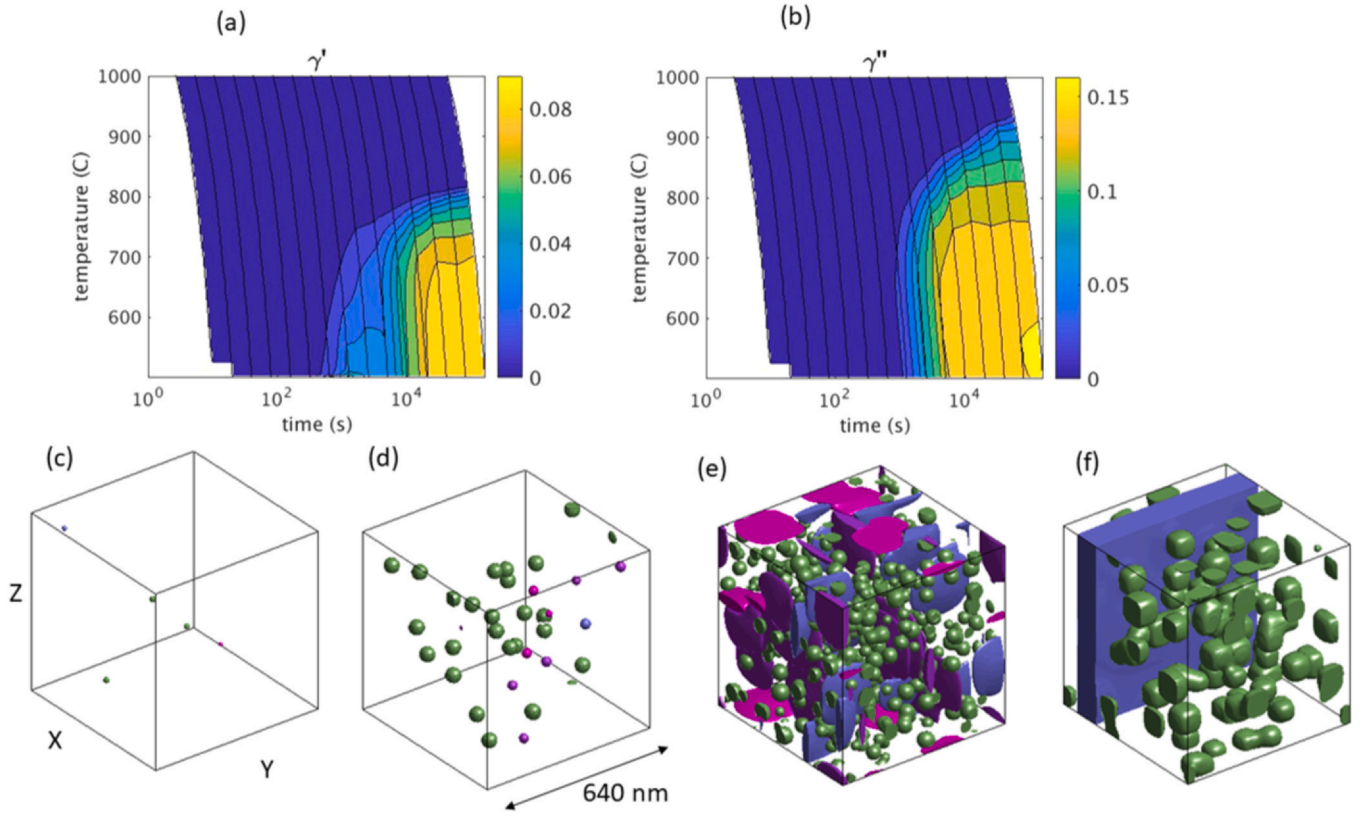

Fig. 5. Calculated CCT diagrams for γ' (a) and γ'' (b) for the bulk RVE. The shades in (a) and (b) represent phase fractions. The precipitate microstructures at the end of continuous cooling for different cooling rates are shown in (c)-(f). The cooling rates are 34 °C/s (c), 2.96 °C/s (d), 0.03 °C/s (e) and 0.0041 °C/s (f). The precipitate microstructures are shown in the basis X || $[100]_{\gamma}$, Y || $[010]_{\gamma}$ and Z || $[001]_{\gamma}$.

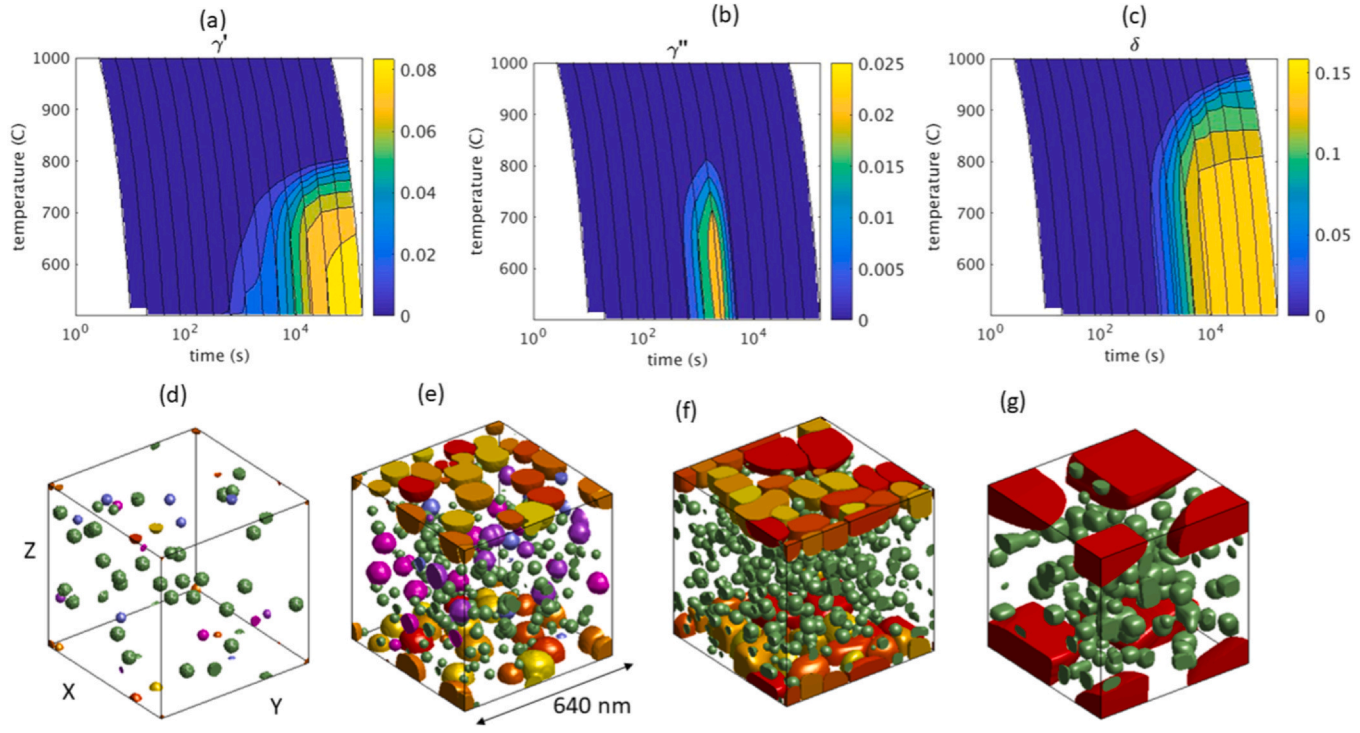

Fig. 6. Computed CCT diagrams for γ' (a) and γ'' (b) and δ (c) for the RVE with grain boundary. The shades in (a), (b) and (c) represent phase fractions. The precipitate microstructures at the end of continuous cooling for different cooling rates are shown in (d)-(g). The cooling rates are 4.25 °C/s (d), 1.04 °C/s (e), 0.03 °C/s (f) and 0.0041 °C/s (g). The precipitate microstructures are shown in the basis X || $[100]_{\gamma}$, Y || $[010]_{\gamma}$ and Z || $[001]_{\gamma}$.

cooling rate 1.04 °C/s, δ precipitates grow from the grain boundary, and γ' and γ'' nucleate and grow in the bulk (Fig. 6c). Fig. 6(f) and (g) show the morphology for slower cooling rates when the equilibrium γ- γ'- δ co-precipitation occurs. The fact that no γ'' forms for slower cooling rates is a consequence of small size of our RVE, and in general, is not consistent with the bulk experimental CCT curve. However, it does represent the behavior in regions close to the grain boundary. This is consistent with the experiments of Geng et al. [35], where a slow cooling of 0.1 °C/min produced coarse γ'' precipitates in the bulk and δ at the grain boundary.

It is evident that while our results are qualitatively consistent with continuous cooling experiments, a quantitative agreement may be difficult to reach. A possible reason for that could be due to the sensitivity of the experimental CCT curves on the processing history or extent of ageing. Available experimental CCT curves [34] are, in fact, not even compatible with the experimental TTT diagrams used for tuning of our nucleation model. Furthermore, the experimental CCT curves also show emerging Laves and Carbide phase, which are not accounted for in the present work.

7. Precipitate evolution under a complex thermal history (rapid thermal cycling)

During an additive manufacturing (AM) process, a sample goes through multiple rapid heating and cooling cycles as different layers of materials are added. The precipitate evolution is expected to be more complex, compared to the continuous cooling case. Not only nucleation and growth, but also dissolution are occurring concurrently during the process.

As an example, we consider three thermal histories of 3600-s duration with oscillation periods of 150 (b), 50 (c) and 25 s (d) and exponentially decaying peak temperature as shown in Fig. 7. The initial temperature is set to 1250 °C and the ambient temperature is equal to 650 °C. In order to isolate the effects of thermal cycling, we also included a case (a) where the temperature decays exponentially without any oscillations. Only the RVE with grain boundary is considered here.

Fig. 8 shows the evolution of the phase fractions. The highest cooling rates associated with our thermal cycles are close to 50 °C/s (d), 25 °C/s (d) and 8.3 °C/s (b). From the simulated CCT curves in Section 5, it is clear that for these cooling rates, no precipitation is expected. However, Fig. 8 shows clearly that precipitates form. By comparing oscillating cases (b-d) with the exponential decay (a), we notice that oscillations speed up the precipitation process. Although heating/cooling rates are nominally fast, a given temperature range is accessed multiple times, and this effect seems to dominate the system behavior. Moreover, faster thermal cycling promotes the formation of γ'' and suppresses the formation of γ' and δ. Note that this is in contrast to the continuous cooling condition as shown in Fig. 5 and Fig. 6 where a faster cooling rate leads to a γ' dominated configuration.

The evolution of precipitates during the cycle (b) is shown in Fig. 9. We notice that complete dissolution of precipitates does not occur during heating, even at high temperatures, as evidenced by an isolated γ'' precipitate marked by arrows in Fig. 9. The first δ nuclei appears on the grain boundaries already after 217 s. Beyond 1000 s, the evolution of precipitates is dominated by growth with limited nucleation. By 3600 s, the precipitates have undergone coarsening, although the precipitates still appear to be equiaxed.

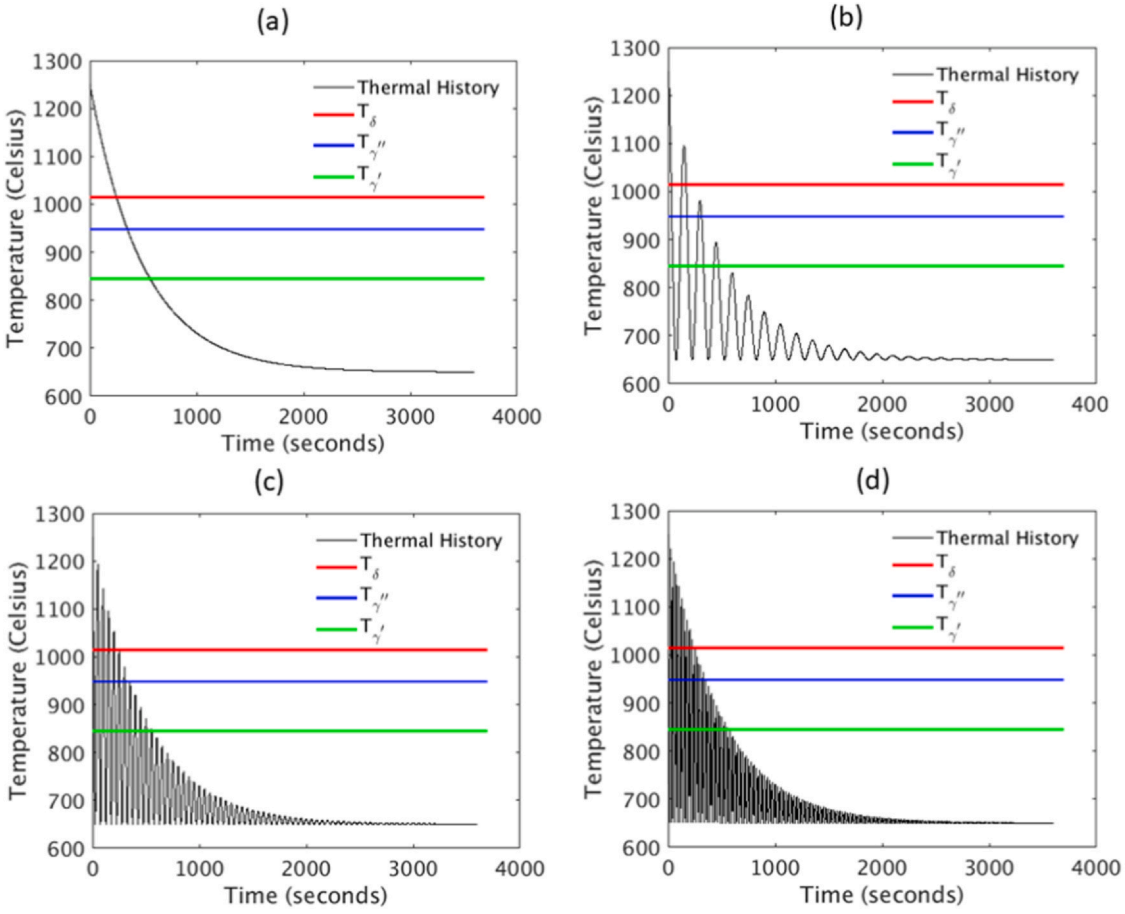

Fig. 7. Temperature evolution for the studied thermal histories. a) pure exponential decay, b) oscillation period 150 s, c) oscillation period 50 s, and d) oscillation period 25 s.

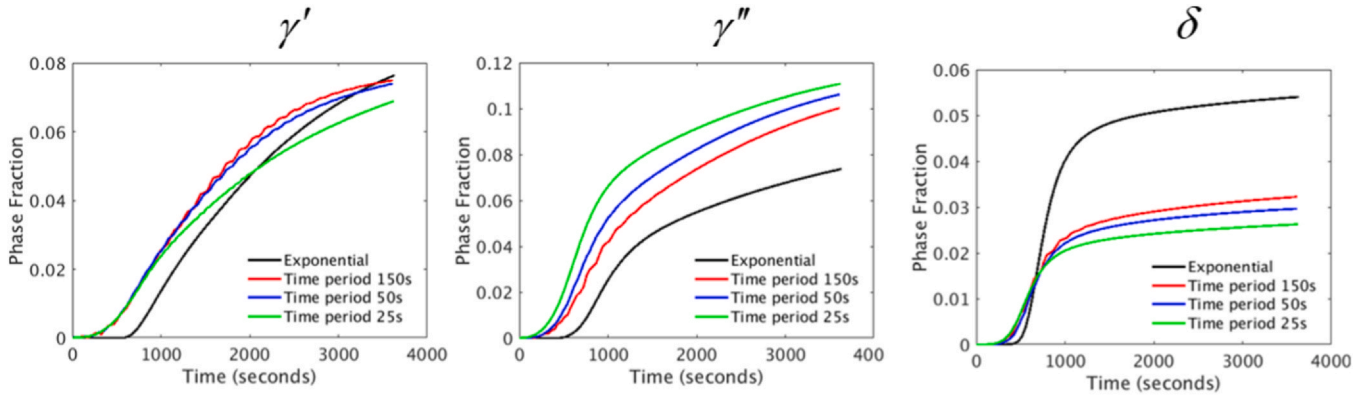

Fig. 8. Evolution of the precipitate phase fractions for the thermal histories from Fig. 6.

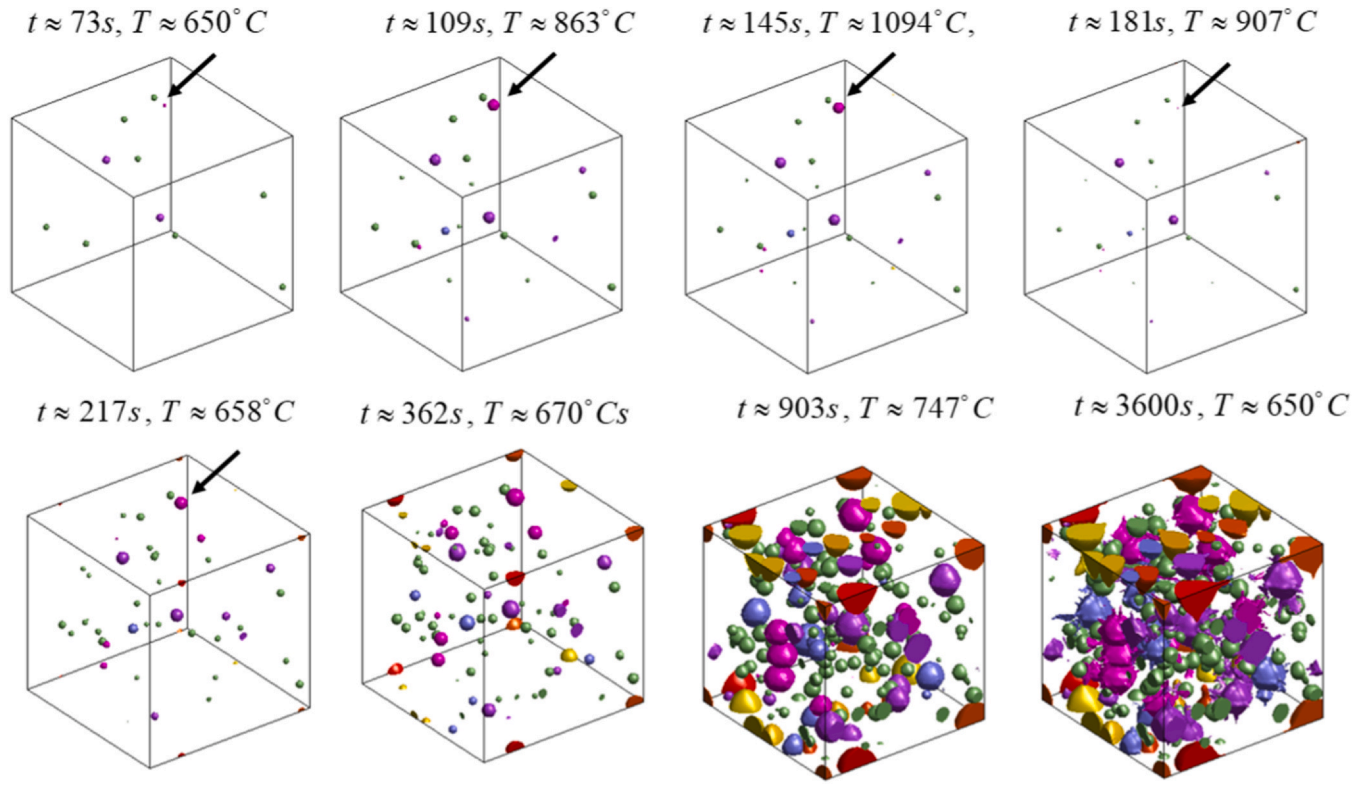

Fig. 9. Evolution of the precipitates for the cycle with time period 150 s. The arrows show the evolution of a selected precipitate during the early stages of the cycle.

Since the thermal cycles are fast, it is not easy to in-situ examine the precipitate evolution in experiments. However, such attempts are being made, for example, in a recent work related to high γ' CMS-X4 super-alloy [36]. We are not aware of any experimental studies that examine the influence of such repetitive thermal cycles on the precipitation process in IN718, which is a much more complex alloy. Interestingly, Jouiad and co-workers [37] experimentally studied the effect of a single heating/cooling cycle on the precipitate microstructures in IN718. Similar to our prediction, it was found that the cycling promoted the precipitation of γ''.

8. Summary and conclusions

This paper presents a phase field framework to predict the precipitate evolution of multi-phase alloys during arbitrary thermal histories. The framework incorporates thermodynamic and kinetic data obtained from CALPHAD and the classical nucleation model, which is parametrized using existing experimental TTT diagrams.

As a demonstration, we chose nickel based super-alloy IN718. We show that the nucleation model indeed can be parametrized such that the calculated TTT diagrams reproduce the experimental TTT with good quantitative agreement. The calculated CCT characteristics are also consistent with existing experiments. The parametrization of PFM model was then used to predict the microstructure evolution under different thermal histories resembling typical AM processes. Our simulations demonstrate that thermal cycling can lead to preferential growth of certain phases in multi-phase alloys. In particular case of IN718 we show that faster thermal cycling promotes the formation of γ'' and suppresses the formation of γ' and δ.

It should be noted that there are certain limitations in the present framework. For example, we apply a surrogate ternary Ni-{Al}-{Nb} thermodynamic model to formulate IN718. Therefore, phases, such as Laves and carbides, are not included. Under fast cooling conditions, these phases are known to form [25]. Also, the present model does not consider the possible intragranular nucleation of δ precipitates that may occur from γ'' precipitates. Extensions of the

surrogate composition approximation and the classical nucleation model to address these issues may constitute the future development of the present PFM framework.

CRediT authorship contribution statement

Robert Laskowski: conceptualization, methodology, software, investigation, writing – original draft, writing – review editing, **Kun Wang:** methodology, writing – original draft, writing – review editing, validation. **Rajeev Ahluwalia:** conceptualization, methodology, investigation, writing - original draft, writing – review editing. **Kewu Bai:** methodology, writing – review editing. **Guglielmo Vastola:** project management, conceptualization, writing – review editing. **Yong-Wei Zhang:** funding acquisition, conceptualization, writing – review editing.

Declaration of Competing Interest

The authors declare that they have no known competing financial interests or personal relationships that could have appeared to influence the work reported in this paper.

Acknowledgments

The grant support from Advanced Manufacturing Engineering Industrial Alignment Fund Pre-Positioning Program (No. A19E1a0097, A1893a0031) and the National Supercomputing Centre (NSCC) Singapore for the usage of supercomputing facilities are gratefully acknowledged. J. Mikula and L Athanasius are acknowledged for discussions and technical assistance.

Appendix A. Supporting information

Supplementary data associated with this article can be found in the online version at doi:10.1016/j.jallcom.2021.158630.

References

[1] J.J. Ruan, N. Ueshima, K. Oikawa, Growth behavior of the delta-Ni3Nb phase in superalloy 718 and modified KJMA modeling for the transformation-time-temperature diagram, J. Alloy. Compd. 814 (2020) 152289.
[2] X. Chen, N. Xiao, D. Li, G. Li, D. Sun, The finite element analysis of austenite decomposition during continuous cooling in 22mnB5 steel, Model. Simul. Mater. Sci. Eng. 22 (2014) 065005.
[3] C. Murgau, R. Pederson, L.E. Lindgren, A model for Ti-6Al-4V microstructure evolution for arbitrary temperature changes, Model. Simul. Mater. Sci. Eng. 20 (2012) 055006.
[4] K. Wu, F. Zhang, S. Chen, W. Cao, Y.A. Chang, A Modeling Tool for the Precipitation Simulations of Superalloys During Heat Treatments, in: R.C. Reed, K.A. Green, P. Caron, T.P. Gabb, M.G. Fahrmann (Eds.), Proceedings of the International Symposium on Superalloys, The Minerals, Metals and Materials Society, Warrendale, PA, USA, 2008, pp. 933–939 2008.
[5] N. Saunders, Z. Guo, X. Li, A.P. Miodownik, J.-Ph Schillé, Using *JMatPro* to model materials properties and behavior, JOM 55 (2003) 60–64..
[6] N. Moelans, B. Blanpain, P. Wollants, An introduction to phase field modeling of microstructural evolution, CALPHAD 32 (2008) 268–294.
[7] Ingo Steinbach, Phase field models in materials science, Model. Simul. Mater. Sci. Eng. 17 (2009) 073001.
[8] N. Zhou, D.C. Lv, H.L. Zhang, D. McAllister, F. Zhang, M.J. Mills, Y. Wang, Computer simulation of phase transformation and plastic deformation in IN718, Acta Mater. 60 (2014) 270–286.
[9] R.P. Shi, D.P. McAllister, N. Zhou, A.J. Detor, R. DiDomizio, M.J. Mills, Y. Wang, Growth behavior of gamma-prime/gamma-double-prime co-precipitates in Ni-Base superalloys, Acta Mater. 164 (2019) 220–236.
[10] Y. Ji, Y. Lou, M. Qu, J.D. Rowatt, Fan Zhang, T.W. Simpson, L.Q. Chen, Predicting coherency loss of gamma_doubleprime precipitates in IN718 superalloy, Metall. Mater. Trans. A 47A (2016) 3235–3247.
[11] R. Ahluwalia, R. Laskowski, N. Ng, M. Wong, S.S. Quek, D.T. Wu, Phase field simulation alpha/beta microstructure in titanium alloy welds, Mater. Res. Express 7 (2020) 046517.
[12] J.P. Simmons, Y. Wen, C. Shen, Y.Z. Wang, Microstructural development involving nucleation and growth phenomena simulated with the phase field model, Mater. Sci. Eng. A 365 (2004) 136–143.
[13] Y. Ji, B. Ghaffari, M. Li, L.Q. Chen, Phase field modeling of theta-prime precipitation kinetics in 319 aluminium alloys, Comput. Mater. Sci. 151 (2018) 84–94.
[14] E.A. Loria eds, Super Alloys 718, 625 and various derivatives, (Warrendale: TMS, the Minerals, Metals and Minerals Society, 1989, 1991, 1994, 1999, 2001 and 2005).
[15] J.W. Brooks, P.J. Bridges, Metallurgical stability of Inconel Alloy 718, Superalloys 1988 (1988) 33–42.
[16] M.C. Chaturvedi, Y.F. Han, Strengthening mechanisms in Inconel 718 superalloy, Metal Sci. 17 (1983) 145–149.
[17] M. Sundarraman, P. Mukhopadhay, S. Bannerjee, Precipitation of the delta Ni_3Nb phase in two nickel based superalloys, Metall. Trans. A 19 (1988) 453–465.
[18] S. Azadian, L.Y. Wei, R. Warren, Delta phase precipitation in Inconel 718, Mater. Charact. 53 (2004) 7–16.
[19] Kirman, Warrington, The precipitation of Ni3Nb phases in a Ni-Fe-Cr-Nb alloy, Metall. Trans. 1 (1970) 2667–2675.
[20] R.G. Thomson, J. Dobbs, D. Mayo, The effect of heat treatment in microfissuring in Alloy 718, Weld. J. 65 (1986) 299–304.
[21] A. Oradei-Basile, J.F. Radavich, A current TTT diagram for wrought alloy 718, in: E.A. Loria (Ed.), Superalloys 718, 625 and Various Derivatives, TMS, 1991, pp. 325–335.
[22] H. Chandler, Heat Treater's Guide: Practices and Pro-cedures for Nonferrous Alloys, ASM International, USA, 1996 ISBN 0-87170-565-6.
[23] M.J. Anderson, C. Panwisawas, Y. Sovani, R.P. Turner, J.W. Brooks, H.C. Basoalto, Mean field modelling of the intermetallic precipitate phases during heat treatment and additive manufacturing of Inconel 718, Acta Mater. 156 (2018) 432–445.
[24] H.C. Basoalto, C. Panwisawas, Y. Sovani, M.J. Anderson, R.P. Turner, B. Saunders, J.W. Brooks, A computational study on the three-dimensional printability of precipitate-strengthened nickel-based superalloys, Proc. R. Soc. A Math. Phys. Eng. Sci. 474 (2018) 20180295.
[25] C. Kumara, A. Segerstark, F. Hanning, N. Dixit, S. Joshi, J. Moverare, P. Nylen, Microstructure modeling of laser metal powder directed energy deposition of alloy 718, Addit. Manuf. 25 (2019) 357–364.
[26] S.G. Kim, W.T. Kim, T. Suzuki, Phase field model for binary alloys, Phys. Rev. B 60 (1999) 7186–7197.
[27] J.O. Andersson, J. Agren, Models for numerical treatment of multicomponent diffusion, J. Appl. Phys. 72 (1992) 1350–1355.
[28] F. Zhang, W. Cao, C. Zhang, S. Chen, J. Zhu, D. Lv (2018) Simulation of Co-precipitation Kinetics of γ' and γ'' in Superalloy 718. In: Ott E. et al. (eds) Proceedings of the 9th International Symposium on Superalloy 718 & Derivatives: Energy, Aerospace, and Industrial Applications. The Minerals, Metals & Materials Series. Springer, Cham. ⟨https://doi.org/10.1007/978-3-319-89480-5_8⟩.
[29] ⟨https://materialsproject.org/⟩.
[30] J.D. Robson, M.J. Jones, P.B. Prangnell, Extension of the N-model to predict competing homogeneous and heterogeneous nucleation, Acta Mater. 51 (2003) 1453–1468.
[31] J. Svodoba, F.D. Fischer, P. Fratzl, E. Kozechnik, Modeling of kinetics in multi-component multi-phase systems with spherical precipitates I: Theory, Mater. Sci. Eng. A 385 (2004) 166–174.
[32] C. Slama, A. Abdellaoui, Structural characterization of the aged Inconel 718, J. Alloy. Compd. 306 (2000) 277–284.
[33] C. Slama, C. Servant, G. Cizeron, Aging of the Inconel 718 alloy between 500 and 750°C, J. Mater. Res. 12 (1997) 2298–2316.
[34] C.I. Garcia, D.E. Camus, E.A. Loria, A.J. DeArdo, Thermomechanical processing and continuous cooling transformation behavior of IN718, Superalloys (1992) 527–536.
[35] L. Geng, Y.S. Na, N.K. Park, Continuous cooling transformation behavior of Alloy 718, Mater. Lett. 30 (1997) 401–405.
[36] B. Wahlmann, F. Galgon, A. Stark, S. Gayer, N. Schell, P. Staron, C. Korner, Growth and coarsening kinetics of gamma prime precipitates in CMSX-4 under simulated additive manufacturing conditions, Acta Mater. 180 (2019) 84–96.
[37] M. Jouiad, E. Marin, R.S. Devarapalli, J. Cormier, F. Ravaux, C. Le Gall, J.M. Franchet, Microstructure and mechanical properties evolutions of alloy 718 during isothermal and thermal cycling over-aging, Mater. Des. 102 (2016) 284–296.